Journal of Power Sources 662 (2026) 238655

Contents lists available at ScienceDirect

Journal of Power Sources

journal homepage: www.elsevier.com/locate/jpowsour

Coarse-grained physics-based modelling for tape casting of fuel-electrode supports in Solid Oxide Cells

Tan Le-Dinh [a,b,c], Mohammed Alabdali [a,b], Franco M. Zanotto [a,b], Hartmut Schlenz [c], Norbert H. Menzler [c,d], Olivier Guillon [c,d,e], Alejandro A. Franco [a,b,f,g,*]

[a] Laboratoire de Réactivité et de Chimie des Solides, UMR CNRS 7314, Université de Picardie Jules Verne, F-80039, Amiens Cedex 1, France
[b] Réseau sur le Stockage Electrochimique de l'Energie (RS2E), Hub de l'Energie, FR CNRS 3459, 15 rue Baudelocque, 80039 Amiens Cedex, France
[c] Forschungszentrum Jülich GmbH, Institute of Energy Materials and Devices (IMD), IMD-2: Materials Synthesis and Processing, 52428 Jülich, Germany
[d] RWTH Aachen, Institute of Mineral Engineering, 52074 Aachen, Germany
[e] Jülich Aachen Research Alliance: JARA-Energy, Jülich 52425, Germany
[f] ALISTORE-European Research Institute, Hub de l'Energie, FR CNRS 3104, 15 rue Baudelocque, 80039 Amiens Cedex, France
[g] Institut Universitaire de France, 1 rue Descartes, 75231 Paris Cedex 05, France

HIGHLIGHTS

- Discrete Element Method for the fuel-electrode substrate manufacturing.
- Fitted and validated force fields for the solvent-based slurry of the substrate.
- First model to link manufacturing process to physical properties of the green tape.
- Simulated green tape microstructure of the fuel-electrode substrate.
- Cross-sectional views of the calculated green tape are extracted from the DEM model.

ARTICLE INFO

Keywords:
Solid Oxide Cells (SOCs)
Anode substrate
Tape casting
Computational modelling
Discrete Element Method

ABSTRACT

Optimising the tape casting process for fabricating NiO/YSZ cermet-based fuel-electrode supports in Solid Oxide Cells remains a resource-intensive challenge. Improving the green tape properties are often reliant on trial-and-error procedures or proprietary knowledge that is inaccessible to the broader scientific community. In this work, we use computational simulations as a powerful tool to link the manufacturing process to the final microstructure of the tape. A novel three-dimensional physics-based model is presented to simulate the slip preparation and the homogeneous drying process of the tape casting producing the fuel electrode support in Solid Oxide Cells. Our model is well-calibrated to experimental data, and we investigate the dried microstructure of the simulated support.

1. Introduction

In the pursuit of addressing the challenges posed by climate change and the depletion of finite fossil fuel resources, green energy, also known as renewable energy, has emerged as a viable and critical solution in the global energy landscape. Environmentally-friendly energy sources, such as solar, wind, and hydropower, have a crucial role to play in decreasing greenhouse gas emissions. Nevertheless, the intermittent nature of these sources poses challenges in ensuring a stable and reliable energy supply. This results in the need of efficient power generation devices. Amongst them, solid oxide cells (SOCs) stand out as a promising technology that holds a strong potential to boost the energy transition.

SOCs are classified as electrochemical energy conversion devices that can operate sequentially in two distinct modes within one unit. In the solid oxide fuel cell (SOFC) mode, this technology directly transforms the chemical energy of the fuel into electricity. Alternatively, while the conversion of renewable energy (power-to-gas) is taken into account, reversible solid oxide fuel cells (rSOFCs) function as solid oxide electrolysis cells (SOECs). SOCs conventionally operate at high temperatures ranging between 650 °C and 900 °C [1,2]. State-of-the-art

* Correspondence to: Laboratoire de Réactivité et de Chimie des Solides (LRCS), Université de Picardie Jules Verne, Hub de l'Energie, UMR CNRS 7314, 15 rue Baudelocque, 80039 Amiens, France.
E-mail address: alejandro.franco@u-picardie.fr (A.A. Franco).

https://doi.org/10.1016/j.jpowsour.2025.238655
Received 11 July 2025; Received in revised form 14 October 2025; Accepted 19 October 2025
Available online 12 November 2025

SOCs are fundamentally comprised of a dense electrolyte sandwiched between two porous electrodes, *i.e.* an anode (a fuel electrode) and a cathode (an air electrode), where fundamental electrochemical reactions take place. SOCs have particular advantages in terms of energy conversion efficiency and fuel flexibility, allowing them to operate on carbohydrate fuels with internal or external reforming [2,3]. To increase SOC's unit cell efficiency, the electrolyte layer thickness was reduced to approximately 5 – 20 μm [4,5]. As a result, the ohmic loss attributed to the electrolyte thickness is minimised, enabling lower operating temperatures as well as higher power density [6,7]. Furthermore, lowering the operating temperature significantly mitigates degradation (due to corrosion of the ancillary reactant delivery equipment and detrimental effects on the cell), resulting in increased lifetime [8–11]. In order to utilise the thinner electrolyte, fuel-electrode-supported cells (FESCs), also called anode-supported cells, with a planar design were studied at Forschungszentrum Jülich [12,13]. Nevertheless, the expensive cost of these cells along with the shortage of appropriate materials, required for the demanding SOC operation conditions, prevent SOCs from being commercialised [14,15]. Hence, an optimised manufacturing procedure is required to lower the production cost of each SOC's unit. Additionally, selecting an effective fabrication method is essential for developing each component to integrate them into single cells and stacks. For transportation and portable application, achieving microfabricated dimensions through manufacturing is critical to enable simplified designs [16,17].

In FESCs, a fuel-electrode support or a fuel-electrode substrate must exhibit sufficient mechanical strength of the cell. Moreover, the functions of the support are also electrical connection and gas permeability for reactants and products. This results in the major requirements of the fuel-electrode support: high electrical conductivity for electronic conduction and a sufficiently open porous network for gas transport. NiO/YSZ cermets were widely selected as the porous fuel-electrode substrates, as they were reduced to Ni/YSZ cermets in the presence of the fuel during cell start-up, contributing to both sufficient mechanical stability and high electrical conductivity. One of the promising low-cost methods widely used to fabricate the fuel-electrode substrate is the tape-casting method [18,19]. Tape casting is a well-known technique for the formation of thin-flat-ceramic sheets [20]. The mass production of green tape using this promising process demands casting slip preparation, including powders, binders, plasticisers, and dispersants [20,21].

In the tape-casting process, the mechanical and physical attributes of the green tapes are of the utmost importance in the subsequent processing and the final characteristics of the substrate [22]. In order to produce high-quality green tape, a trial-and-error procedure is often applied to ensure the most stable suspension and achieve the desired tape properties [23–25]. Nonetheless, this approach is costly, resulting in material wastage, product rejection, and significant time investment. Besides, understanding the evolution of the three-dimensional (3D) microstructure during the tape casting process is critical for investigating key phenomena such as agglomeration, sedimentation, and particle packing, which significantly impact the porosity and mechanical properties of the final support structure. Advanced visualisation techniques, including focused ion beam-scanning electron microscopy (FIB-SEM) [26–28] and X-ray computed tomography (XCT) [29,30], are frequently utilised to examine the internal microstructure of the electrode. Despite their utility, these techniques can be time-consuming and pose challenges to fully differentiate between material phases.

Computational modelling has been used to understand the influence of electrode microstructure on electrochemical performance. Although most studies rely on stochastically generated electrode microstructures [31–34], the manufacturing process plays a pivotal role in determining the morphology and electrochemical performance of the support in SOCs [35–37]. Thus, accounting for microstructural analysis with manufacturing parameters gives a comprehensive framework, providing deep insights into microstructural evolution.

Table 1
Materials used to prepare the casting slip.

Material	Role in the slip	Producer
NiO	Powder	G. Vogler B.V.
8YSZ	Powder	Imerys
Ethanol	Solvent	Merck
Methyl ethyl ketone	Solvent	Merck
Polyvinyl butyral B-98	Binder	Solutia Inc.
Solusolv S-2075	Plasticiser	Solutia Inc.
PEG400	Plasticiser	Merck
BYK 220 S	Dispersant	BYK

In the context of the ARTISTIC research initiative [38], numerous physics-based numerical models were reported allowing the prediction of the three-dimensional microstructure of battery electrodes as a function of manufacturing parameters [39–44]. These models typically employ coarse-grained molecular dynamics or discrete element method (DEM) simulations for each step in the electrode manufacturing process chain. To the best of our knowledge, this powerful computational approach has yet to be considered in the case of SOC devices. In this article, a physics-based DEM approach is applied to model two stages of the tape-casting process of the fuel-electrode supports, namely the slip phase and its drying. In the slip phase, the DEM approach models the interaction between NiO, 8YSZ, and domains representing the solvent, the binder, the dispersant and the plasticiser (Binder Dispersant Plasticiser Domain—BDPD) to mimic the properties of the casting slip. Subsequently, the experimentally validated simulated slip is used as an input to simulate the drying stage by solvent removal from the BDPD.

In this study, we propose a 3D physics-based modelling framework to simulate the fabrication of fuel-electrode substrates in Ni-cermet planar FESCs. This framework characterises the green tape's microstructural features using the DEM approach, which operates efficiently with limited computational resources. As a proof of concept, the underlying theory and methodology are introduced. An overview of the results obtained and the model perspectives are discussed in details as well. Finally, we conclude and indicate perspectives for our work.

2. Materials and methods

2.1. Casting slip preparation

The most prevalent materials for the support in the state-of-the-art FESCs are Ni-YSZ cermets [45–47]. The NiO (Green Nickel Oxide) and 8YSZ (8 mol% yttria-stabilised zirconia) powders were utilised to attain a 57:43 NiO:8YSZ volume fraction [48]. The NiO and 8YSZ powder mixture, Ethanol and Methyl ethyl ketone solvents, binders, dispersants, plasticisers and grinding balls were mixed for 10 h to form the most stable suspension of the slip. The particle size distributions of both NiO and 8YSZ were not distinguishable in the prepared slip and determined with d_{10} = 0.35–0.45 μm, d_{50} = 0.5–0.7 μm, and d_{90} = 0.8–1.0 μm. Table 1 lists all material components used for the slip preparation.

2.2. Physical model workflow

There are two primary phases in our modelling methodology to simulate the 3D microstructure of the fuel-electrode substrate in the FESCs, which are covered in-depth in this study, namely the slip phase, and its drying phase. More specifically, the DEM approach is employed to simulate the slip and dried microstructures corresponding to each step of the tape casting process of the ceramics. DEM is a computational simulation technique used to model the dynamic behaviour of complex systems at the particle level, such as powders and granular materials by numerically solving Newton's equations of motion for a collection of particles in a simulated system [49,50]. The simulation starts by defining the initial positions, velocities, and forces acting upon each

particle in the system. These initial conditions may be based upon experimental data, previous simulations, or theoretical calculations. The interactions between a pair of particles are described by force fields (FFs), which are mathematical functions that model the potential energy of the system as a function of particle distances. The forces acting upon each particle are calculated based upon their positions by using the force fields. In particular, these forces are determined by the gradients of the potential energy with respect to the particle positions. Newton's second law of motion, then, is used to update the positions and velocities of the particles in the system. The equations of motion are numerically integrated over a small time step so as to calculate the new positions and velocities of the particles based upon the current positions, velocities, and forces. The integration step is left to run until the system reaching the equilibrium, each time advancing the system's state by a small time interval. The smaller the time step, the more accurate the simulation, however, it also increases the computational cost. Particles of all materials are randomly located in a big enough simulation box at the beginning for the purpose of avoiding the overlap of particles. A constant temperature and constant pressure (NPT ensemble) are applied for the slip-phase simulation at 300 K and 1 bar until the system is equilibrated. In this work, LAMMPS [51,52], an open-source molecular dynamics programme, is employed to simulate the slip phase upon the boundary condition being periodic in all three directions (x, y, and z-axis). The drying phase is then simulated by using the experimentally validated simulated slip as an input, which enables the production of the dried microstructure of the fuel-electrode substrate. The dried microstructure is utilised for subsequent analysis steps once the computational simulation is well-calibrated. Fig. 1a illustrates the tape casting process for the support in SOCs highlighting the two stages being simulated: the slip preparation and its drying process. Our computational workflow is illustrated in Fig. 1b.

It is worth mentioning that two types of parameters, namely the manufacturing parameters and the force field (FF) parameters, are required as input for our computational model. The manufacturing parameters are defined as the parameters associated with the experimental process, for instance, the slip solid content (SC) and the particle size distribution of the material. The manufacturing parameters are, as per the experimental conditions, assumed to be constant, for example, SC is constant along the simulation.

The FF parameters, on the other hand, are model-internal parameters specifying how strongly particles interact with one another and thus have a powerful impact on the DEM simulation results. It is, therefore, critical to configure the FF parameters to mimic the properties of the system. The Lennard–Jones FF (LJFF) and Granular Hertz FF (GHFF) are combined to create the FFs that resemble the physicochemical characteristics of the casting slip [53]. The LJFF [54,55] is utilised to imitate an attractive and repulsive interaction between two particles, which is derived from the Lennard–Jones potential energy given as

$$V(r) = 4\epsilon\left[\left(\frac{\sigma}{r}\right)^{12} - \left(\frac{\sigma}{r}\right)^{6}\right] \qquad r < r_c, \tag{1}$$

where ϵ is the well depth that measures the strength of the attraction between the two particles, σ represents the distance of closest approach between the centres of two particles if their potential energy were zero, r_c is the cut-off distance at which the particles stop interacting with one another, and r represents the distance between a pair of particles measured from the centre of one particle to the centre of the other particle.

As mentioned in the previous section, the forces acting upon each particle in the system are calculated as

$$F_{LJ}(r) = -\nabla V(r), \tag{2}$$

where r is the distance between the centre of the two particles.

The GHFF [56,57] is used to handle the mechanical aspects of the system, which is defined as

$$F_{GH} = \sqrt{\delta}\sqrt{\frac{R_i R_j}{R_i + R_j}}\left[\left(k_n \delta n_{ij} - m_{\text{eff}}\gamma_n v_n\right) - \left(k_t \Delta s_t + m_{\text{eff}}\gamma_t v_t\right)\right], \tag{3}$$

where δ is the overlap distance, R_i as well as R_j represent the radius of two particles, k_n is the normal elastic constant, k_t is the tangential elastic constant, γ_n represents the viscoelastic damping constant for normal interaction, γ_t is the viscoelastic damping constant for tangential interaction, v_n and v_t represent the relative velocity of two interacting particles in terms of normal and tangential components, respectively. In addition, Δs_t is the tangential displacement vector between a pair of interacting particles, n_{ij} represents the unit vector along the line linking the centres of the two interacting particles, and m_{eff} is the effective mass of both particles and expressed as

$$m_{\text{eff}} = \frac{m_i m_j}{m_i + m_j}, \tag{4}$$

where m_i and m_j are the mass of particle i and particle j, respectively.

It is evident from Eq. (3) that F_{GH} will be equal to 0 for $\delta = 0$. An appropriate proportion of overlap between interacting particles must thus be permitted so as to account for the GHFF. Another important parameter, the coefficient of friction (μ), determined by the highest ratio between the tangential and normal forces, is the last factor required for the simulation [57].

It should be noted that the LJFF in this study is an approximation to describe the interaction between particles, and we chose LJ because of its simplicity. Specifically, the LJ was used as an approach to control the distance and interaction forces amongst different particles. This adjustment of interparticle distances is critical to stabilise the particles in both the slip and drying phases and to prepare a physically plausible particle packing for the GH contact model, which governs elastic and frictional forces once particles are in contact. By contrast, the GH contact model is directly derived from physical contact mechanics and represents the particle-level physics, ensuring suspension stability and particle packing after drying that are consistent with experimental observations. Therefore, these two FFs form the coarse-grained description, allowing the model to mimic the experimentally observed suspension behaviour, particle packing, and microstructural features of the fuel-electrode support. While the LJFF provides an effective means to mimic mesoscale cohesive interactions, the GHFF preserves rigorous particle-level physics, enabling the overall DEM framework to be considered physics-based in the coarse-grained modelling sense.

In the simulation, the particles are explicitly considered as distinct material kinds in the system, i.e. NiO, 8YSZ, and BDPD, in which the BDPD particle is a type of effective particle representing also the solvent and the organic materials in the slip. It is worth noting that all particles were modelled as effective spheres. All forces are calibrated to fit the experimental output descriptors. Specifically, the slip phase is validated by comparing the experimental with the simulated density. Additionally, such DEM simulations should also display a calibration of the viscosity of the simulated slip. As a proof of concept, the calibration of two viscosity points is required to ensure that the simulated slip behaves in agreement with the experimental one. A series of non-equilibrium simulations was adopted to determine multiple viscosity values against the desired shear rates. This was accomplished by reversly rotating the upper and lower planes of the simulation box with respect to the x direction and thus deforming the simulation box in a single lateral direction. The length of the simulation box multiplied by the selected shear rate in the y direction determines the deformation rate. Besides, it is also necessary to allow enough time for the simulation to converge on the target viscosity value. Our non-equilibrium simulations were deployed by running 10^7 timesteps with a size of

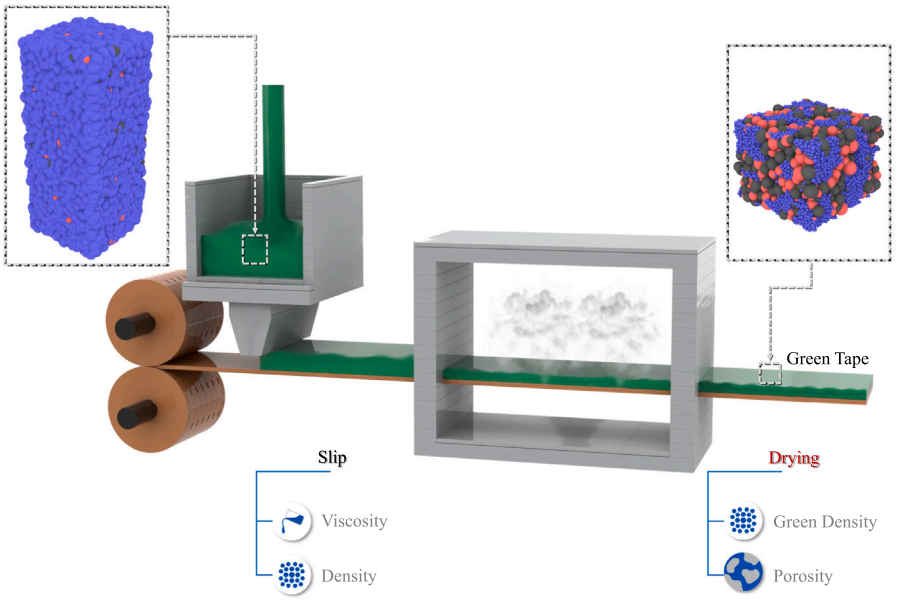

(a)

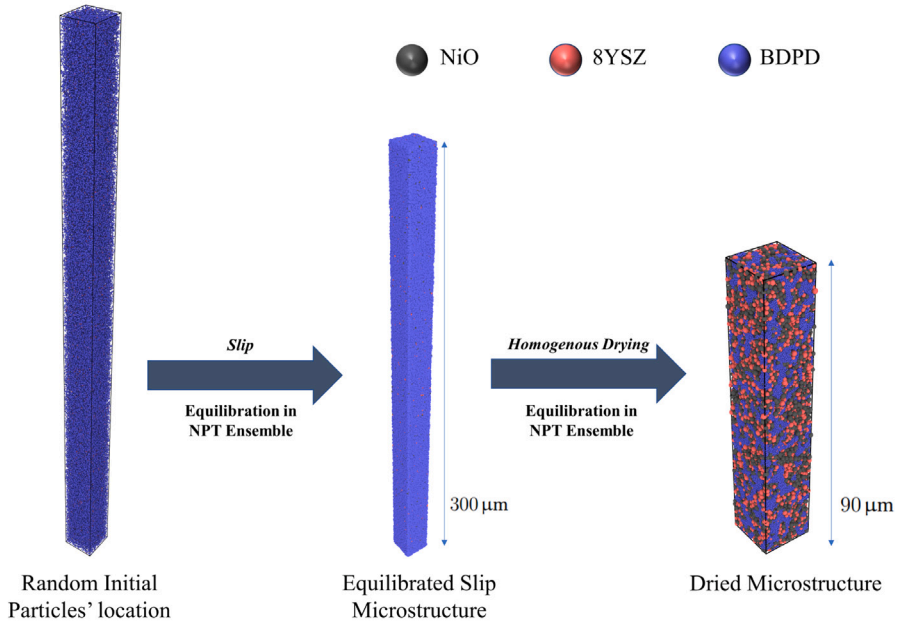

(b)

Fig. 1. (a) A diagram illustrating the stages of the tape casting process of a SOC fuel-electrode support. (b) A schematic snapshot of our computational workflow depicting each simulation step in this work. The workflow starts with an initial configuration consisting in a random spatial distribution of particles. Afterwards, the slip microstructure is obtained by performing the simulation until the initial structure is equilibrated in the NPT ensemble. Grey spheres represent NiO, light red particles illustrate 8YSZ, and slate-blue spheres exhibit Binder Dispersant Plasticiser Domain (BDPD). In the slip phase, NiO and 8YSZ are almost obscured by the BDPD including the solvent. Furthermore, the image also shows the dried microstructure obtained after solvent removal by shrinking the BDPD spheres in order to mimic the solvent evaporation. We performed several simulations following this workflow to ensure proper statistical representativeness. Videos displaying the evolution of the simulations, highlighting solvent removal, are included in the Supplemental Information. The particle size distribution used for the simulation can also be found in the Supplemental Information. (For interpretation of the references to colour in this figure legend, the reader is referred to the web version of this article.)

$\Delta t = 0.001$ µs. The simulated viscosity was, then, calculated by taking the mean of the instantaneous viscosity measurements following the convergence of the simulation. The same FF parameter values of the slip simulation were used for viscosity simulation to ensure consistency. Our viscosity calibration was performed on a small slip microstructure (14 162 particles). After the calibration of the viscosity achieved the experimental values, the model was scaled up to 226 568 particles to meet the expected thickness.

Regarding the drying stage, the drying model is modelled by the homogeneous shrinkage of BDPD particles mimicking the solvent evaporation. Specifically, all the BDPD particles, containing the solvent, were instantly shrunk from 1.8 µm to 0.38 µm in diameter. The DEM simulation continued to run until reaching the equilibrium. The FFs

were re-calibrated to obtain a dried microstructure satisfying the experimental porosity and density. Stronger particle connections formed by binder bridges, along with improved mechanical properties of the green tape, result from increased attractive and elastic interactions. The difference trnalsated in the values of FFs of the drying and slip phases. Consequently, the thickness drops from top to bottom. Throughout the simulation, the temperature persists constant at 300 K at each time step.

The simulation domain sizes were chosen to ensure that each system contained a sufficient number of particles to simulate the SC used in the experiment. The sizes of the simulation domain must also be consistent with the experimental physical properties of the substrate. Besides, these simulation domain sizes should represent a balance between computational cost and the physical representativeness of the substrate system. In this work, for each phase, two domain sizes were employed: a larger domain regarding the experimentally measured thickness for the slip or the corresponding dried microstructure, providing the validation of the simulated microstructure, and a smaller domain used as a representative test case to assess finite-size effects. The small and large domains of the slip simulation were approximately $L_x \times L_y \times L_z = 13 \times 13 \times 32$ μm^3 and $L_x \times L_y \times L_z = 17 \times 17 \times 300$ μm^3, respectively. The corresponding small and large domains for the dried microstructures were approximately $L_x \times L_y \times L_z = 12 \times 12 \times 9$ μm^3 and $L_x \times L_y \times L_z = 16 \times 16 \times 90$ μm^3, respectively. Simulations for both small and large domain sizes showed no significant differences in agreement with our experimental measurements, confirming that finite-size effects are negligible. All information on FF parameters about the slip and drying phases can be found in the Supplemental Information.

3. Results and discussion

The DEM approach was conducted using LAMMPS software to model the slip and drying phases of the tape-casting process of fuel-electrode substrates in SOCs. All the simulations were run on the MatriCS High Performance Computing cluster of the Université de Picardie Jules Verne, in Amiens, France, using one node with 128 GB of RAM and 2 processors (Intel® Xeon® CPU E5-2680 v4 @ 2.40 GHz, 28 cores) [58]. Simulating the large microstructure, comprising 226 568 particles, required approximately 78 h for the slip stage and 226 h for the drying stage, while simulations of the smaller microstructure, containing 14 162 particles, completed in approximately 10, 14, and 29 h for the slip, viscosity, and drying stages, respectively. In order to further optimise the models and assess the physicochemical aspects of the slip simulation, the BDPD diameter and its density are taken into account. The interaction amongst these material particles was controlled by the FF parameters, which were parameterised to imitate the experimental properties. In other words, all FF parameters were calibrated to achieve a simulated density value within the experimental uncertainty range. Specifically, the experimental casting-slip density value of 2.23 g/cm^3 is utilised to validate the calculated slip microstructure with a simulated density of 2.22 g/cm^3. Furthermore, the rheological properties of the casting slip also have an effect on the fabrication of the substrate [59,60]. It is, therefore, important to ensure that the simulated slip behaves like the experimental one. The casting slip should behave as if a shear-thinning fluid, also known as a pseudoplastic fluid, operates [61,62], which means that the casting slip exhibits a decreasing apparent viscosity with an increasing shear rate [63,64]. Even though a full viscosity curve is desirable, this would be too computationally expensive and two viscosity values are determined to be sufficient for this proof-of-concept study. To meet this requirement, manually tuning the FFs to obtain two viscosity values corresponding to low and high shear rates was performed. The simulated viscosities corresponding to the chosen shear rates are shown in Table 2, and the animation of the simulation is provided as a video in the Supplemental Information.

Table 2
Experimental and simulated viscosity as a function of the shear rate.

Shear rate (s^{-1})	Viscosity (Pa s)	
80 ± 0.3	Experiment	1.7 ± 0.3
	Simulation	1.9 ± 0.2
100 ± 0.3	Experiment	1.5 ± 0.3
	Simulation	1.6 ± 0.1

In the drying phase, the porosity calibration is used as a means to validate the DEM model. The experimental porosity of the green sample is calculated as

$$\phi_{\text{exp}}\,(\%) = \frac{V_{\text{pore}}}{V_{\text{green tape}}} \times 100\%, \tag{5}$$

where V_{pore} is the pore volume of the green sample, and $V_{\text{green tape}}$ is the volume of the green sample.

It is critical to ensure the stability and reproducibility of the DEM simulations to validate the reliability of the generated data. Regarding this, six different simulations (Slip Microstructure 1–6) were conducted for the slip phase by varying the initial positions of the particles, number of particles in the simulation box, and the size of the simulation box, providing various microstructures for the analysis to ensure the consistency of the microstructural properties and particle arrangement of our model. Subsequently, these slip microstructures served as inputs to generate the dried microstructures (Dried Microstructures 1–6) in the drying phase. The density and porosity of these dried microstructures were calculated to ensure the stability and consistency of the DEM model, achieving the values of 3.45 ± 0.01 g/cm^3 for the green density, and 9.7 ± 0.3 % for the porosity, in good agreement with those of the experiment which are 3.46 g/cm^3 and 9.6% for the green density and porosity, respectively. All information pertaining to these simulated microstructures can be found in the Supplemental Information (Table S2).

Radial Distribution Function (RDF) was adopted to evaluate the microstructural characteritics of the slip and dried microstructures. As a robust analytical tool, RDFs enable the evaluation of structural consistency in the microstructures across various simulation runs by implementing a quantitative measurement for comparing particle arrangements in a 3D microstructure during the simulation. Figs. 2 and 3 depict the RDF analyses in the slip and drying phases. Fig. 2 demonstrates the RDF curves of six different slip microstructures in terms of three different scenarios, namely NiO-8YSZ pair-correlation (Fig. 2a), NiO-NiO pair-correlation (Fig. 2b), and 8YSZ-8YSZ pair-correlation (Fig. 2c). Likewise, Fig. 3 shows the corresponding RDF curves for the dried microstructures in terms of four different scenarios: pair-correlation for all particle types (Fig. 3a), NiO-8YSZ pair-correlation (Fig. 3b), NiO-NiO pair-correlation (Fig. 3c), and 8YSZ-8YSZ pair-correlation (Fig. 3d). In the slip stage, solid particles, such as NiO and 8YSZ, are suspended in a liquid phase. This is also explained in the simulation when most solid spheres were covered by the BDPD overlapped highly to effectively mimic the behaviour of viscous suspensions such as the slip (Fig. 1b). In other words, BDPD particles serve as a liquid phase surrounding the solid particles in the slip phase, which results in the relative distribution of NiO and 8YSZ particles being the main object investigated in the slip stage. By contrast, in the drying stage, BDPD particles tend to cluster after solvent removal to function as binder bridges, which enables stronger particle bonds as well as a higher level of stiffness. Hence, BDPD was taken into consideration along with NiO and 8YSZ particles during the drying stage. Overall, RDFs indicate consistency during the microstructural evolution in both slip and drying steps. The RDF curves for each type of particle interactions are nearly identical regarding different microstructures within each phase. Nevertheless, the differences between RDFs are smaller in the

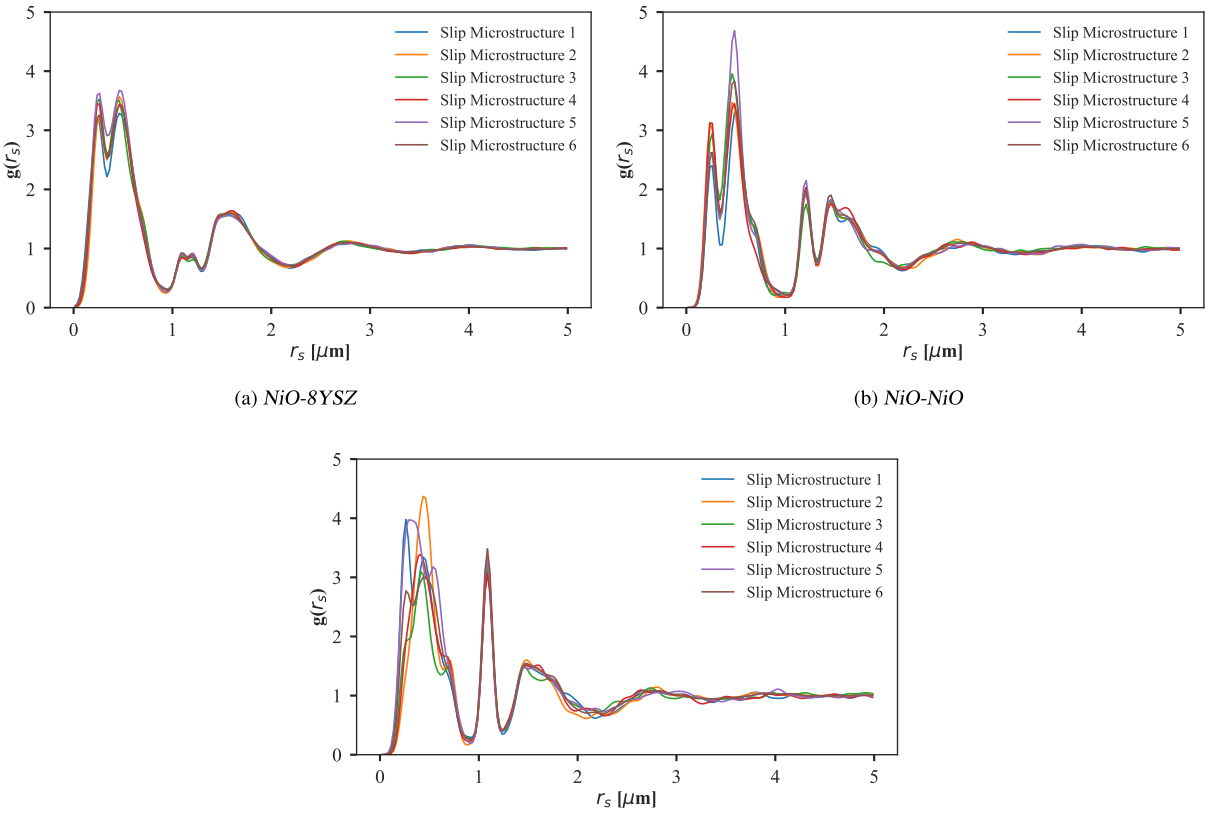

(a) *NiO-8YSZ* (b) *NiO-NiO*

(c) *8YSZ-8YSZ*

Fig. 2. Pair-wise radial distribution functions (RDFs) for 6 different slip microstructures with respect to all cases: (a) NiO-8YSZ, (b) NiO-NiO, and (c) 8YSZ-8YSZ. The first peaks in all RDFs are quite high, demonstrating that NiO and 8YSZ particles cluster at short distances within the slip. Comparative analysis of the RDFs confirms the co-existence of both particle types in close proximity. Particularly, in the case of NiO-NiO correlations, the first peak is slightly lower than the second peak, attributable to the intervening presence of 8YSZ particles at shorter radial distances from the reference NiO particle. g(r) tends to unity at long distances indicating that the particles are well dispersed throughout the microstructure—characteristic behaviour of a stabilised casting slip system.

drying phase. This explains the difference in NiO and 8YSZ particle distribution where there is a higher particle movement in the slip phase in comparison to the dry phase. Furthermore, the consistency shown by RDFs also ensures the confidence of the DEM model regardless of the initial particle configurations or model size, which supports the reproducibility and reliability of our model.

To further characterise the dried microstructure, we analysed the simulated thick dried microstructure (90 μm in thickness, composed of 226 568 particles). The volume fraction for each material phase in z-axis (*i.e.* along the thickness) is shown in Fig. 4. Overall, Fig. 4 illustrates a consistent trend of the volume fraction distribution of all material phases, which is critical for fabricating the green tape. Specifically, NiO and 8YSZ occupy the majority of the volume fraction of the dried microstructure. While the volume fraction of NiO decreases, the volume fraction of 8YSZ increases along the thickness from bottom to top of the dried microstructure. This demonstrates the interaction between the NiO and 8YSZ particles during the formation of the dried microstructure. The trend for the volume fraction distribution of the BDPD phase reflects an homogeneous distribution of binders and additives throughout the dried microstructure. The volume fraction of the pores remains low along the thickness of the dried microstructure. Fig. 5 demonstrates cross-sectional views of the dried microstructure of the fuel-electrode support obtained from our DEM simulation at various depths. Specifically, the cross section of the dried microstructure was extracted along the thickness direction after voxelising the 3D dried microstructure of the simulated support by using an in house Python script. It is clear that the cross-sectional microstructures show that the phases, including NiO (green), 8YSZ (yellow), BDPD (dark purple), and pore (dark blue), are well-distributed within the examined slices, which aligns with the distribution of the volume fraction of each phase. Moreover, the cross-sectional views show the tight arrangement of the particles within the examined slices. These cross-sectional views indicate the correlations between NiO and 8YSZ particles along the thickness of the dried microstructure. The cross-sectional views also demonstrate the role of BDPD as the binder bridges for the NiO and 8YSZ particles as we discussed above. These characterisations of phases in the examined simulated dried microstructure are also affirmed by calculating the coordination number to provide an idea of particle packing and connectivity after solvent evaporation in the tape-casting process (Fig. 6). Indeed, Fig. 6a and 6b show strong spatial correlations between the NiO and 8YSZ phases. This implies NiO and 8YSZ particles were well-mixed during the slip preparation and remained uniformly distributed after drying, which is an important characteristic for ensuring mechanical stability as well as enhancing connectivity in the final microstructure for the next manufacturing step, the sintering process. Meanwhile, the coordination number of BDPD exhibits a uniform distribution along the microstructure (Fig. 6c and 6f). The high values (*i.e.* orange or red) correspond to tight particle arrangement in the examined area due to the presence of the binder phase (BDPD). Furthermore, BDPD forms a network connected along the microstructure reflecting the role of BDPD in supporting the connection between particles, which is of the utmost importance in the formation of a stable microstructure. Besides, a Pore Network Model (PNM) is shown in Fig. 7. To investigate the pore structures as well as their distribution, the diverse shapes of pores are approximated as

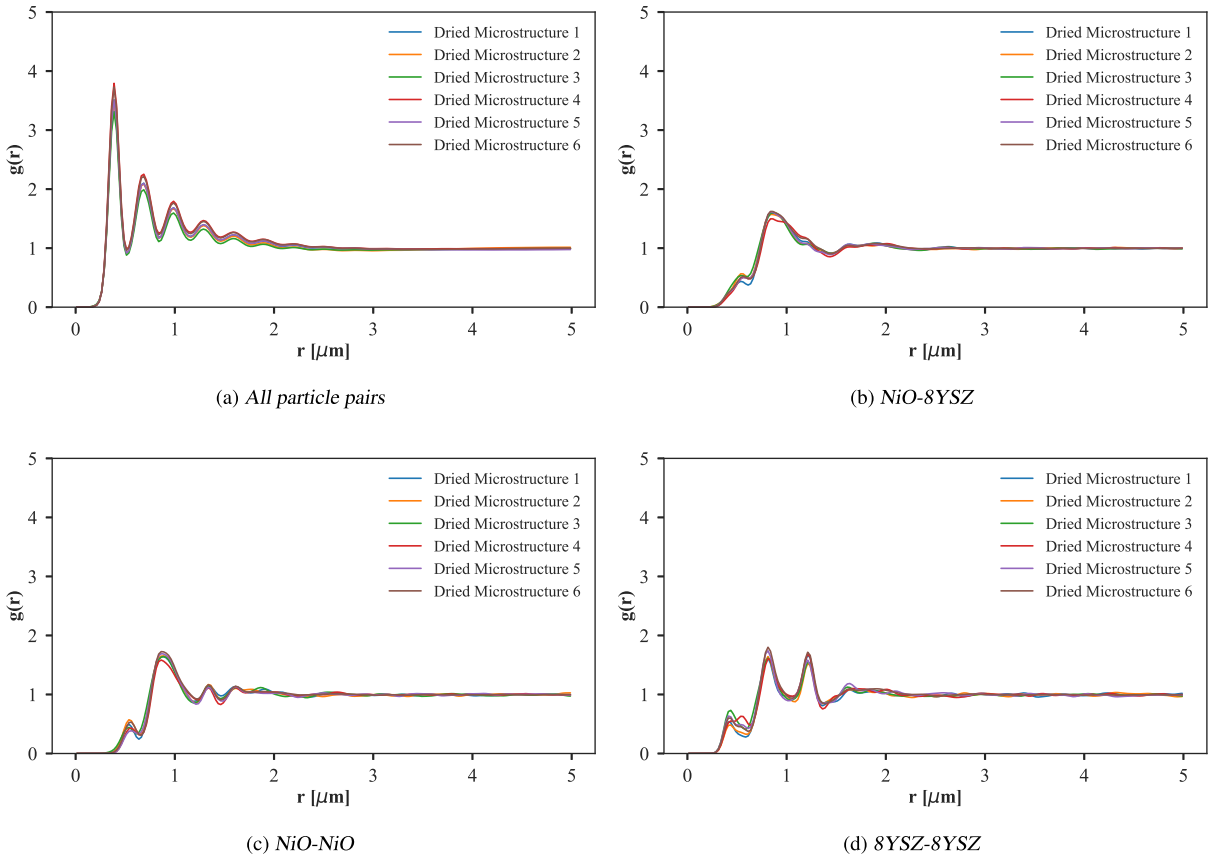

(a) *All particle pairs* (b) *NiO-8YSZ*

(c) *NiO-NiO* (d) *8YSZ-8YSZ*

Fig. 3. Pair-wise RDFs for the dried microstructures corresponding to their slip microstructures with respect to all cases: (a) All particle pairs, (b) NiO-8YSZ, (c) NiO-NiO, and (d) 8YSZ-8YSZ. RDFs of the dried microstructures demonstrate a stable particle configuration, characterised by distinct primary peaks that gradually decay to $g(r) = 1$ beyond radial distances of approximately 2.5 μm, which demonstrates transition to homogeneous particle distributions at longer distance. In general, RDFs reveal significant differences between the slip and dried microstructures, highlighting structural changes in particle distribution as the system transitions from the slip phase to the drying phase.

spheres for simplification by using the Avizo software (Thermo Fisher Scientific) [65]. Specifically, Fig. 7 illustrates the distribution of pores along the thickness of the calculated microstructure of the green tape. PNM shows that the size of the pores in the simulated microstructure is up to 2.5 μm. Along the microstructure, there is a homogeneous distribution of pores, where each pore is approximately 2 μm in size. Meanwhile, larger pores are located closer to the central section of the simulated green tape. A well-optimised pore arrangement in the dried microstructure of the fuel-electrode support in FESCs facilitates the formation of a favourable microstructure after the sintering process. This helps to ensure efficient gas transport, a high density of triple-phase boundaries, and improved fuel utilisation. It also contributes to mechanical robustness during sintering, which is critical for long-term cell performance.

SEM and tomography characterisations can provide valuable insights into the green tape microstructure of the fuel-electrode support, yet their application at this early stage is often limited due to technical constraints. Our model provides a valuable first step in visualising features that are difficult to observe through experimental imaging, particularly the distribution of materials with low imaging contrast. It therefore serves as a useful complement to direct imaging and supports an integrated modelling and experimental approach for gaining deeper insights into how manufacturing processes influence material distribution and final properties. Besides, the DEM-generated dried microstructure, representing the green body of the fuel-electrode support, can also serve as the starting point for multiscale modelling.

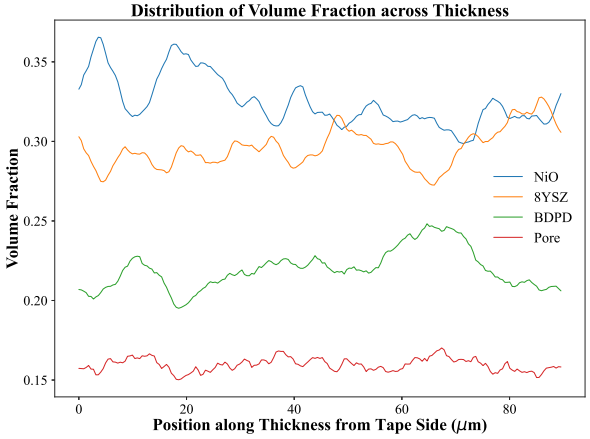

Fig. 4. Volume fraction evolutions of NiO, 8YSZ, BDPD and pores along the thickness of the dried substrate microstructure.

Specifically, it can be used as input for a phase-field model to simulate sintering. The resulting sintered microstructures can then be employed in subsequent performance-oriented simulations (e.g., Lattice

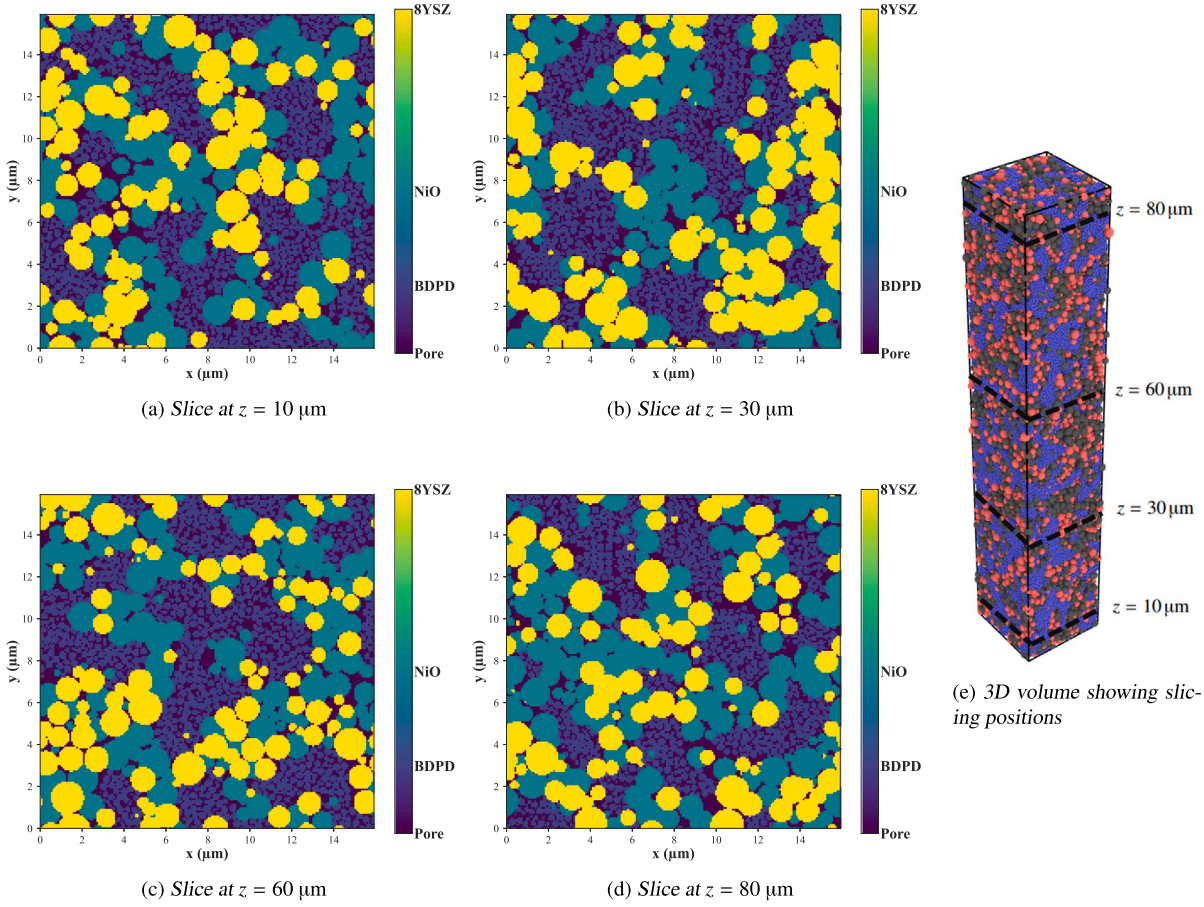

(a) *Slice at* $z = 10$ µm (b) *Slice at* $z = 30$ µm

(c) *Slice at* $z = 60$ µm (d) *Slice at* $z = 80$ µm

(e) *3D volume showing slicing positions*

Fig. 5. Cross-sectional views of the dried microstructure (90 µm in thickness) resulting from our simulation, shown in the xy plane (*i.e.* along the thickness direction), at various depths: (a) Slice at $z = 10$ µm, (b) Slice at $z = 30$ µm, (c) Slice at $z = 60$ µm, and (d) Slice at $z = 80$ µm. Each colour represents a different phase, namely NiO, 8YSZ, BDPD, and pore. (e) 3D volume showing slicing positions, providing an overview of the simulated volume and the planes where the cross-sections (a–d) were taken. (For interpretation of the references to colour in this figure legend, the reader is referred to the web version of this article.)

Boltzmann method, pore network modelling) or thermo-mechanical durability studies (e.g., based on finite element methods).

4. Conclusions and perspectives

In this article, a physics-based computational workflow, based upon DEM, to simulate the tape casting process of a SOC fuel-electrode support made of NiO/8YSZ cermet is presented for the first time. The model was calibrated with in house experimental data, such as the slip density, the viscosity of the slip, the density and the porosity of the green tape so as to reproduce the experimental conditions as closely as possible. Our model describes two main stages in the tape casting process of the fuel-electrode support, namely the slip casting and its drying. Our performed DEM simulations allow linking each step of the tape-casting process to the 3D-resolved microstructure of the support, by verifying its properties for good agreement with experimental data. This allows for an efficient and more physics-based approach than those based upon stochastic generation of microstructures. A homogeneous distribution of all materials throughout the dried microstructure was observed from the simulation, which is expected to happen in practice before the heat treatment of the green tape.

Our model employs a homogeneous drying assumption for the BDPD particles, which is a simplification of the actual drying behaviour. While this represents an approximation, it is sufficient in the context of this proof-of-concept study to capture the main trends of the tape casting and drying processes. The debinding and sintering of the materials helps control the porosity and avoid undesirable pore clustering after the sintering process. These processes, not considered in this first modelling proof of concept, enhance both the mechanical performance and electrochemical properties of the support [66].

The work reported herein further exhibits that the ARTISTIC workflow can be applied not only to batteries but also to other technologies such as SOCs. Nevertheless, our framework can be extended to also simulate properties involved in other processing steps of SOC supports as well as functional layers, such as the sintering process. It is useful, as a future perspective, to complement our findings with supplementary imaging characterisation to provide better insights related to material processing/performance coupling. Even though our model has some limitations due to its assumptions (e.g. consideration of spherical particles), it provides, to the best of our knowledge, the most complete computational approach to connect manufacturing with the microstructure properties. It also remains particularly well suited to investigate, from a physical perspective, the tape casting process. By using our experimentally validated computational workflow, numerous combinations of the manufacturing parameters may be researched to inspect quickly the material processability before performing the experimental fabrication. This results in a powerful computational approach for the generation, with physics background, of component microstructures utilised in a wide spectrum of energy conversion applications.

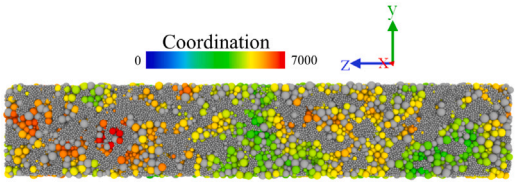

(a) *Coordination number of NiO (with all particles)*

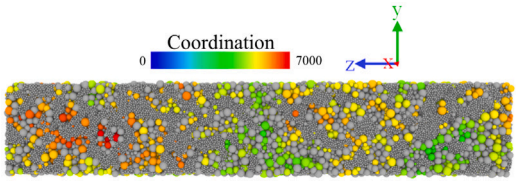

(b) *Coordination number of 8YSZ (with all particles)*

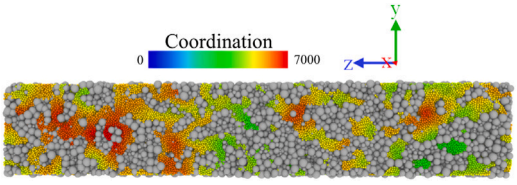

(c) *Coordination number of BDPD (with all particles)*

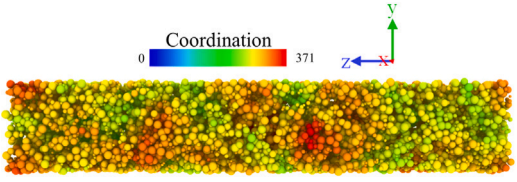

(d) *Coordination number of NiO-NiO particles*

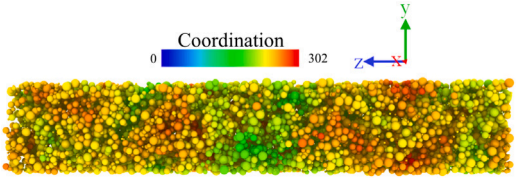

(e) *Coordination number of 8YSZ-8YSZ particles*

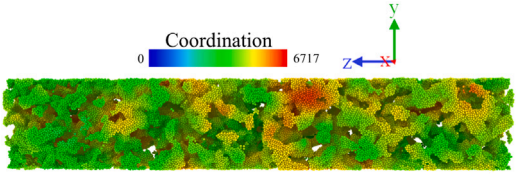

(f) *Coordination number of BDPD-BDPD particles*

Fig. 6. Coordination number of particles in the dried microstructure. The colour code exhibits the reference particles, such as (a) NiO, (b) 8YSZ, (c) BDPD. The rest of particles in contact with the reference particles are shown in grey. The colour zone exhibits only the reference particles in contact with each other, such as (d) NiO-NiO particles, (e) 8YSZ-8YSZ particles, (f) BDPD-BDPD particles. (For interpretation of the references to colour in this figure legend, the reader is referred to the web version of this article.)

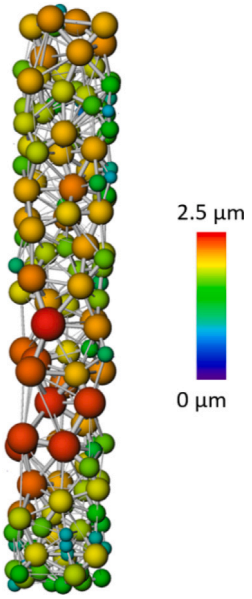

Fig. 7. Pore Network Model of the dried microstructure for the SOC support, illustrating the pore distribution and size throughout the dried microstructure. The colour bar indicates equivalent pore diameters, while the throats indicate the pore interconnections. (For interpretation of the references to colour in this figure legend, the reader is referred to the web version of this article.)

CRediT authorship contribution statement

Tan Le-Dinh: Writing – original draft, Visualization, Validation, Software, Methodology, Investigation, Formal analysis, Data curation, Conceptualization. **Mohammed Alabdali:** Writing – review & editing, Validation, Methodology, Conceptualization. **Franco M. Zanotto:** Writing – review & editing, Validation, Software. **Hartmut Schlenz:** Writing – review & editing, Supervision. **Norbert H. Menzler:** Writing – review & editing, Supervision. **Olivier Guillon:** Writing – review & editing, Supervision, Project administration, Funding acquisition. **Alejandro A. Franco:** Writing – review & editing, Supervision, Project administration, Methodology, Funding acquisition, Conceptualization.

Declaration of competing interest

The authors declare that they have no known competing financial interests or personal relationships that could have appeared to influence the work reported in this paper.

Acknowledgements

T.L.D and A.A.F acknowledge the Region Hauts-de-France and Université de Picardie Jules Verne for the funding support. A.A.F., M.A. and F.M.Z. acknowledge the European Union's Horizon Europe research and innovation program under Grant Agreement No. 101069686 (PULSE-LiON). T.L.D, H.S., N.H.M., and O.G. acknowledge Forschungzentrum Jülich GmbH for the support. T.L.D., H.S., N.H.M., O.G. and A.A.F. gratefully acknowledge funding by the Federal Ministry of Economic Affairs and Energy of Germany (Bundesministerium für Wirtschaft und Energie, Project-No.: 03EI3085 A, ML4SOC). The authors acknowledge Ralf Kauert and Eugen Susakin for the preparation of the slip and the green tape used for the extraction of the experimental data used in this work. A.A.F.acknowledges the Institut Universitaire de France for the support.

Appendix A. Supplementary data

Supplementary material related to this article can be found online at https://doi.org/10.1016/j.jpowsour.2025.238655.

Data availability

Data will be made available on reasonable request.

References

[1] F. Han, R. Mücke, T.V. Gestel, A. Leonide, N.H. Menzler, H.P. Buchkremer, D. Stöver, Novel high-performance solid oxide fuel cells with bulk ionic conductance dominated thin-film electrolytes, J. Power Sources 218 (2012) http://dx.doi.org/10.1016/j.jpowsour.2012.06.087.

[2] S. He, Y. Zou, K. Chen, S.P. Jiang, C.P.S. Jiang, A critical review of key materials and issues in solid oxide cells, Interdiscip. Mater. 2 (2023) 111–136, http://dx.doi.org/10.1002/IDM2.12068.

[3] C. Lenser, D. Udomsilp, N.H. Menzler, P. Holtappels, T. Fujisaki, L. Kwati, H. Matsumoto, A.G. Sabato, F. Smeacetto, A. Chrysanthou, S. Molin, 9 - solid oxide fuel and electrolysis cells, in: O. Guillon (Ed.), Advanced Ceramics for Energy Conversion and Storage, in: Elsevier Series on Advanced Ceramic Materials, Elsevier, 2020, pp. 387–547, http://dx.doi.org/10.1016/B978-0-08-102726-4.00009-0.

[4] N. Menzler, F. Tietz, S. Uhlenbruck, H. Buchkremer, D. Stöver, Materials and manufacturing technologies for solid oxide fuel cells, J. Mater. Sci. 45 (2010) 3109–3135, http://dx.doi.org/10.1007/s10853-010-4279-9.

[5] L. Blum, H.-P. Buchkremer, S. Gross, A. Gubner, L.G.J.B. de Haart, H. Nabielek, W.J. Quadakkers, U. Reisgen, M.J. Smith, R. Steinberger-Wilckens, R.W. Steinbrech, F. Tietz, I.C. Vinke, Solid oxide fuel cell development at forschungszentrum Juelich, Fuel Cells 7 (3) (2007) 204–210, http://dx.doi.org/10.1002/fuce.200600039.

[6] S. Sarner, A. Schreiber, N.H. Menzler, O. Guillon, Recycling strategies for solid oxide cells, Adv. Energy Mater. 12 (35) (2022) 2201805, http://dx.doi.org/10.1002/aenm.202201805.

[7] T.T. N.Q. Minh, Science and Technology of Ceramic Fuel Cells, ELSEVIER Science, 2011.

[8] F. Tietz, H.P. Buchkremer, D. Stöver, Components manufacturing for solid oxide fuel cells, Solid State Ion. 152–153 (2002) 373–381, http://dx.doi.org/10.1016/S0167-2738(02)00344-2.

[9] A.K. Padinjarethil, F.R. Bianchi, B. Bosio, A. Hagen, Electrochemical characterization and modelling of anode and electrolyte supported solid oxide fuel cells, Front. Energy Res. 9 (2021) 668964, http://dx.doi.org/10.3389/FENRG.2021.668964.

[10] S.M. Majhi, S.K. Behura, S. Bhattacharjee, B.P. Singh, T.K. Chongdar, N.M. Gokhale, L. Besra, Anode supported solid oxide fuel cells (SOFC) by electrophoretic deposition, Int. J. Hydrog. Energy 36 (2011) 14930–14935, http://dx.doi.org/10.1016/J.IJHYDENE.2011.02.100.

[11] A review of solid oxide fuel cell component fabrication methods toward lowering temperature, Int. J. Energy Res. 44 (2020) 594–611, http://dx.doi.org/10.1002/ER.4907.

[12] L. Blum, L.G. de Haart, J. Malzbender, N. Margaritis, N.H. Menzler, Anode-supported solid oxide fuel cell achieves 70 000 hours of continuous operation, Energy Technol. 4 (2016) http://dx.doi.org/10.1002/ente.201600114.

[13] D. Udomsilp, C. Lenser, O. Guillon, N.H. Menzler, Performance benchmark of planar solid oxide cells based on material development and designs, Energy Technol. 9 (2021) http://dx.doi.org/10.1002/ente.202001062.

[14] Z. Shao, S.M. Halle, A high-performance cathode for the next generation of solid-oxide fuel cells, Nature 431 (2004) http://dx.doi.org/10.1038/nature02863.

[15] J. Jeong, S.W. Baek, J. Bae, A diesel-driven, metal-based solid oxide fuel cell, J. Power Sources 250 (2014) 98–104, http://dx.doi.org/10.1016/J.JPOWSOUR.2013.10.100.

[16] C.C. Chao, C.M. Hsu, Y. Cui, F.B. Prinz, Improved solid oxide fuel cell performance with nanostructured electrolytes, ACS Nano 5 (2011) 5692–5696, http://dx.doi.org/10.1021/nn201354p.

[17] P.I. Cowin, C.T. Petit, R. Lan, J.T. Irvine, S. Tao, Recent progress in the development of anode materials for solid oxide fuel cells, Adv. Energy Mater. 1 (2011) 314–332, http://dx.doi.org/10.1002/AENM.201100108.

[18] C. Fu, S.H. Chan, Q. Liu, X. Ge, G. Pasciak, Fabrication and evaluation of Ni-GDC composite anode prepared by aqueous-based tape casting method for low-temperature solid oxide fuel cell, Int. J. Hydrog. Energy 35 (2010) 301–307, http://dx.doi.org/10.1016/J.IJHYDENE.2009.09.101.

[19] M. Letilly, O. Joubert, M.T. Caldes, A.L.G.L. Salle, Tape casting fabrication, co-sintering and optimisation of anode/electrolyte assemblies for SOFC based on BIT07-Ni/BIT07, Int. J. Hydrog. Energy 37 (2012) 4346–4355, http://dx.doi.org/10.1016/J.IJHYDENE.2011.11.140.

[20] E.R.T. Richard E. Mistler, Tape Casting: theory and Practice, The American Ceramic Society, Westerville, OH, 2000.

[21] S.D. Kim, S.H. Hyun, J. Moon, J.H. Kim, R.H. Song, Fabrication and characterization of anode-supported electrolyte thin films for intermediate temperature solid oxide fuel cells, J. Power Sources 139 (2005) 67–72, http://dx.doi.org/10.1016/J.JPOWSOUR.2004.07.013.

[22] M. Descamps, G. Ringuet, D. Leger, B. Thierry, Tape-casting: Relationship between organic constituents and the physical and mechanical properties of tapes, J. Eur. Ceram. Soc. 15 (1995) 357–362, http://dx.doi.org/10.1016/0955-2219(95)90360-U.

[23] J.H. Kim, H. Ko, D.H. Yeo, Z. Park, U. Kumar, K.H. Yoo, A. Nasridinov, S.B. Cho, A versatile strategy for hybridizing small experimental and large simulation data: A case for ceramic tape-casting process, Mater. Des. 234 (2023) http://dx.doi.org/10.1016/j.matdes.2023.112357.

[24] M. Jabbari, R. Bulatova, A.I. Tok, C.R. Bahl, E. Mitsoulis, J.H. Hattel, Ceramic tape casting: A review of current methods and trends with emphasis on rheological behaviour and flow analysis, Mater. Sci. Eng.: B 212 (2016) 39–61, http://dx.doi.org/10.1016/J.MSEB.2016.07.011.

[25] D. Gardini, M. Deluca, M. Nagliati, C. Galassi, Flow properties of PLZTN aqueous suspensions for tape casting, Ceram. Int. 36 (2010) 1687–1696, http://dx.doi.org/10.1016/J.CERAMINT.2010.03.011.

[26] U. Doraswami, P. Shearing, N. Droushiotis, K. Li, N.P. Brandon, G.H. Kelsall, Modelling the effects of measured anode triple-phase boundary densities on the performance of micro-tubular hollow fiber SOFCs, in: Solid State Ionics, 192, 2011, http://dx.doi.org/10.1016/j.ssi.2009.10.013.

[27] L. Holzer, B. Münch, B. Iwanschitz, M. Cantoni, T. Hocker, T. Graule, Quantitative relationships between composition, particle size, triple phase boundary length and surface area in nickel-cermet anodes for Solid Oxide Fuel Cells, J. Power Sources 196 (2011) http://dx.doi.org/10.1016/j.jpowsour.2010.08.006.

[28] N. Vivet, S. Chupin, E. Estrade, T. Piquero, P.L. Pommier, D. Rochais, E. Bruneton, 3D microstructural characterization of a solid oxide fuel cell anode reconstructed by focused ion beam tomography, J. Power Sources 196 (2011) http://dx.doi.org/10.1016/j.jpowsour.2011.03.060.

[29] P.R. Shearing, J. Gelb, N.P. Brandon, X-ray nano computerised tomography of SOFC electrodes using a focused ion beam sample-preparation technique, J. Eur. Ceram. Soc. 30 (2010) http://dx.doi.org/10.1016/j.jeurceramsoc.2010.02.004.

[30] K.N. Grew, A.A. Peracchio, W.K. Chiu, Characterization and analysis methods for the examination of the heterogeneous solid oxide fuel cell electrode microstructure: Part 2. quantitative measurement of the microstructure and contributions to transport losses, J. Power Sources 195 (2010) http://dx.doi.org/10.1016/j.jpowsour.2010.07.006.

[31] E.M. Ryan, P.P. Mukherjee, Mesoscale modeling in electrochemical devices—A critical perspective, 71, 2019, http://dx.doi.org/10.1016/j.pecs.2018.11.002.

[32] Y. Suzue, N. Shikazono, N. Kasagi, Micro modeling of solid oxide fuel cell anode based on stochastic reconstruction, J. Power Sources 184 (2008) http://dx.doi.org/10.1016/j.jpowsour.2008.06.029.

[33] M. Neumann, J. Staněk, O.M. Pecho, L. Holzer, V. Beneš, V. Schmidt, Stochastic 3D modeling of complex three-phase microstructures in SOFC-electrodes with completely connected phases, Comput. Mater. Sci. 118 (2016) http://dx.doi.org/10.1016/j.commatsci.2016.03.013.

[34] Y. Zhang, M. Yan, Y. Wan, Z. Jiao, Y. Chen, F. Chen, C. Xia, M. Ni, High-throughput 3D reconstruction of stochastic heterogeneous microstructures in energy storage materials, Npj Comput. Mater. 5 (2019) http://dx.doi.org/10.1038/s41524-019-0149-4.

[35] H. Mohebbi, O. Sharifi, M. Golmohammad, A. Molla Ahmad, The effect of process parameters on the apparent defects of tape-cast SOFC half-cell, Adv. Ceram. Prog. 5 (4) (2019) 12–16, http://dx.doi.org/10.30501/acp.2019.103585.

[36] B. Timurkutluk, M.D. Mat, Effects of anode fabrication parameters on the performance and redox behavior of solid oxide fuel cells, J. Power Sources 258 (2014) http://dx.doi.org/10.1016/j.jpowsour.2014.02.023.

[37] B. Timurkutluk, S. Dokuyucu, The role of tape thickness on mechanical properties and performance of electrolyte supports in solid oxide fuel cells, Ceram. Int. 44 (2018) http://dx.doi.org/10.1016/j.ceramint.2018.06.205.

[38] ERC artistic, 2022, https://www.erc-artistic.eu/. (Accessed 26 April 2022).

[39] T. Lombardo, J.B. Hoock, E.N. Primo, A.C. Ngandjong, M. Duquesnoy, A.A. Franco, Accelerated optimization methods for force-field parametrization in battery electrode manufacturing modeling, Batter. Supercaps 3 (2020) 721–730, http://dx.doi.org/10.1002/BATT.202000049.

[40] T. Lombardo, A.C. Ngandjong, A. Belhcen, A.A. Franco, Carbon-binder migration: A three-dimensional drying model for Lithium-Ion battery electrodes, Energy Storage Mater. 43 (2021) 337–347, http://dx.doi.org/10.1016/J.ENSM.2021.09.015.

[41] T. Lombardo, F. Caro, A.C. Ngandjong, J.B. Hoock, M. Duquesnoy, J.C. Delepine, A. Ponchelet, S. Doison, A.A. Franco, The ARTISTIC online calculator: Exploring the impact of Lithium-Ion battery electrode manufacturing parameters interactively through your browser, Batter. Supercaps 5 (2022) e202100324, http://dx.doi.org/10.1002/BATT.202100324.

[42] A.C. Ngandjong, T. Lombardo, E.N. Primo, M. Chouchane, A. Shodiev, O. Arcelus, A.A. Franco, Investigating electrode calendering and its impact on electrochemical performance by means of a new discrete element method model: Towards a digital twin of Li-Ion battery manufacturing, J. Power Sources 485 (2021) 229320, http://dx.doi.org/10.1016/J.JPOWSOUR.2020.229320.

[43] M. Alabdali, F.M. Zanotto, M. Duquesnoy, A.K. Hatz, D. Ma, J. Auvergniot, V. Viallet, V. Seznec, A.A. Franco, Three-dimensional physical modeling of the wet manufacturing process of solid-state battery electrodes, J. Power Sources 580 (2023) http://dx.doi.org/10.1016/j.jpowsour.2023.233427.

[44] D. Weitze, F.M. Zanotto, D.Z. Dominguez, A.A. Franco, Simulating solid-state battery cathode manufacturing via wet-processing with resolved active material geometries, Energy Storage Mater. 73 (2024) 103747, http://dx.doi.org/10.1016/J.ENSM.2024.103747.

[45] S.Z. Golkhatmi, M.I. Asghar, P.D. Lund, A review on solid oxide fuel cell durability: Latest progress, mechanisms, and study tools, Renew. Sustain. Energy Rev. 161 (2022) 112339, http://dx.doi.org/10.1016/J.RSER.2022.112339.

[46] D. Mohanty, J.Y. Hung, Y.W. Chen, I.M. Hung, Y.R. Lin, Optimization and characterization of porous Ni/YSZ anode microstructure for solid oxide fuel cell, Ceram. Int. (2025) http://dx.doi.org/10.1016/J.CERAMINT.2025.02.021.

[47] M. Lira, N. Kostretsova, I. Babeli, L. Bernadet, S. Marquez, A. Morata, M. Torrell, A. Tarancón, Large-area 3D printed electrolyte-supported reversible solid oxide cells, Electrochim. Acta 467 (2023) http://dx.doi.org/10.1016/j.electacta.2023.143074.

[48] W. Schafbauer, N.H. Menzler, H.P. Buchkremer, Tape casting of anode supports for solid oxide fuel cells at Forschungszentrum Jülich, Int. J. Appl. Ceram. Technol. 11 (2014) 125–135, http://dx.doi.org/10.1111/J.1744-7402.2012.02839.X.

[49] S. Barbhuiya, A. Jivkov, B.B. Das, A review of multi-scale modelling of concrete deterioration: Fundamentals, techniques and perspectives, Constr. Build. Mater. 406 (2023) http://dx.doi.org/10.1016/j.conbuildmat.2023.133472.

[50] C.-W. Hong, Computer-aided process design for forming of pore-gradient membranes, 1997, http://dx.doi.org/10.1016/b978-044482548-3/50006-8.

[51] LAMMPS molecular dynamics simulator, 2025, https://www.lammps.org/#gsc.tab=0. (Accessed 01 July 2025).

[52] A.P. Thompson, H.M. Aktulga, R. Berger, D.S. Bolintineanu, W.M. Brown, P.S. Crozier, P.J. in 't Veld, A. Kohlmeyer, S.G. Moore, T.D. Nguyen, R. Shan, M.J. Stevens, J. Tranchida, C. Trott, S.J. Plimpton, LAMMPS - a flexible simulation tool for particle-based materials modeling at the atomic, meso, and continuum scales, Comp. Phys. Comm. 271 (2022) 108171, http://dx.doi.org/10.1016/j.cpc.2021.108171.

[53] T. Lombardo, F. Lambert, R. Russo, F.M. Zanotto, C. Frayret, G. Toussaint, P. Stevens, M. Becuwe, A.A. Franco, Experimentally validated three-dimensional modeling of organic-based sodium-ion battery electrode manufacturing, Batter. Supercaps 5 (2022) e202200116, http://dx.doi.org/10.1002/BATT.202200116.

[54] J.E. Lennard-Jones, Cohesion, Proc. Phys. Soc. 43 (5) (1931) 461, http://dx.doi.org/10.1088/0959-5309/43/5/301.

[55] pair_style lj/cut command – lammps documentation.

[56] K. Johnson, K. Kendall, A. Roberts, Surface energy and contact of elastic solids, Proc. R. Soc. A: Math. Phys. Eng. Sci. 324 (1971) 301–313, http://dx.doi.org/10.1098/rspa.1971.0141.

[57] pair_style granular command – lammps documentation.

[58] MatriCS plateform, 2022, https://www.matrics.u-picardie.fr/en/documentation-2/partitions/. (Accessed 26 April 2022).

[59] S. Sridhar, U.B. Pal, Effect of slurry properties on anode cermets for solid oxide fuel cells, Powder Technol. 88 (1996) http://dx.doi.org/10.1016/0032-5910(96)03114-2.

[60] C.G. Fonseca, R.M. Basaglia, M.C. Brant, T. Matencio, R.Z. Domingues, Study of the rheological behavior of an anode slurry and the microstructural properties of an anode functional film obtained by spray coating, Powder Technol. 192 (2009) http://dx.doi.org/10.1016/j.powtec.2009.01.022.

[61] T. Liu, C. Ren, Y. Zhang, Y. Wang, L. Lei, F. Chen, Solvent effects on the morphology and performance of the anode substrates for solid oxide fuel cells, J. Power Sources 363 (2017) http://dx.doi.org/10.1016/j.jpowsour.2017.07.110.

[62] A.I. Tok, F.Y. Boey, Y.C. Lam, Non-Newtonian fluid flow model for ceramic tape casting, Mater. Sci. Eng.: A 280 (2000) http://dx.doi.org/10.1016/S0921-5093(99)00691-7.

[63] A. Yahia, S. Mantellato, R.J. Flatt, Concrete rheology: A basis for understanding chemical admixtures, Sci. Technol. Concr. Admixtures (2016) 97–127, http://dx.doi.org/10.1016/B978-0-08-100693-1.00007-2.

[64] Y. Nakayama, Characteristics of a fluid, Introd. To Fluid Mech. (2018) 9–24, http://dx.doi.org/10.1016/B978-0-08-102437-9.00002-4.

[65] Avizo software | materials characterization software - FR, (n.d.), 2022, https://www.thermofisher.com/de/de/home/electron-microscopy/products/software-em-3d-vis/avizo-software.html. (Accessed 26 April 2022).

[66] F. Ternero, L.G. Rosa, P. Urban, J.M. Montes, F.G. Cuevas, Influence of the total porosity on the properties of sintered materials—a review, Metals 11 (2021) http://dx.doi.org/10.3390/met11050730.